Available online at www.sciencedirect.com
SCIENCE DIRECT®
International Journal of Heat and Mass Transfer 48 (2005) 2955–2969
International Journal of HEAT and MASS TRANSFER
www.elsevier.com/locate/ijhmt

Investigation of flow boiling in horizontal tubes: Part I—A new diabatic two-phase flow pattern map

Leszek Wojtan, Thierry Ursenbacher, John R. Thome *

Laboratory of Heat and Mass Transfer (LTCM), Faculty of Engineering Science (STI), Ecole Polytechnique Fédérale de Lausanne (EPFL), CH-1015 Lausanne, Switzerland

Received 6 July 2004
Available online 14 April 2005

Abstract

Several important modifications to the flow pattern map of Kattan–Thome–Favrat [J. Heat Transfer 120(1) (1998) 140–147] made, resulting in a significantly new version of the map. Based on the dynamic void fraction measurements described in [Int. J. Multiphase Flow 30 (2004) 125–137], the stratified–wavy region has been subdivided into three subzones: slug, slug/stratified–wavy and stratified–wavy. Furthermore, annular-to-dryout and dryout-to-mist flow transition curves have been added and integrated into the new flow pattern map, identified by distinct trends of the heat transfer coefficient as a function of vapor quality and by flow pattern observations to determine (and then predict) the inception and completion of dryout in horizontal tubes.

Keywords: Two-phase flow; Flow boiling; Flow pattern maps; Flow regimes; Dryout

1. Introduction

An extensive comparison of existing heat transfer models to a complete database covering different flow types by Kattan [3] indicates that only flow boiling heat transfer prediction methods distinguishing between flow regimes should be seriously considered for general use. In response, Kattan–Thome–Favrat [4] proposed a flow pattern oriented heat transfer model, which combines in the final solution the heat transfer coefficients determined for the wetted and the dry fractions of the tube perimeter for stratified types of flow. As the dry angle θ_{dry}, defining the dry tube perimeter, is calculated based on the flow pattern map, the definition of the transition curves between appropriate flow regimes is of principal importance in the prediction of flow boiling heat transfer.

Furthermore, the flow pattern/flow structure heat transfer model for boiling has also been extended very effectively, with appropriate modifications, to intube condensation in horizontal tubes by Thome and coworkers [5,6], where again the flow pattern map and stratification effect are of primary importance. Hence, further improvement of two-phase heat transfer models requires better understanding of the liquid–vapor flow structure of the various flow patterns.

In this light, the objective of the present study was to improve our most recent version of the Kattan et al. [1] flow pattern map based on information obtained from dynamic void fraction measurements and observations

* Corresponding author. Tel.: +41 21 693 5981; fax: +41 21 693 5960.
E-mail address: john.thome@epfl.ch (J.R. Thome).

0017-9310/$ - see front matter © 2005 Elsevier Ltd. All rights reserved.
doi:10.1016/j.ijheatmasstransfer.2004.12.012

Nomenclature

A	cross-sectional area of flow channel, m^2
A_L	cross-sectional area occupied by liquid-phase, m^2
A_{LD}	dimensionless cross-sectional area occupied by liquid-phase
A_V	cross-sectional area occupied by vapor-phase, m^2
A_{VD}	dimensionless cross-sectional area occupied by vapor-phase
D	internal tube diameter, m
D_{ext}	external tube diameter, m
Fr_L	liquid Froude number $[G^2/(\rho_L^2 gD)]$
Fr_V	vapor Froude number $[G^2/(\rho_V^2 gD)]$; Mori et al. [15] used $[G^2/(\rho_V(\rho_L-\rho_V)gD)]$;
g	gravitational acceleration, 9.81 m/s^2
G	mass velocity of liquid plus vapor, kg/m^2s
G_{dryout}	dryout transition mass velocity, kg/m^2s
G_{mist}	mist flow transition mass velocity, kg/m^2s
G_{strat}	stratified flow transition mass velocity, kg/m^2s
G_{wavy}	wavy flow transition mass velocity, kg/m^2s
h_L	vertical height of liquid, m
h_{LD}	dimensionless vertical height of liquid
h_{LV}	latent heat of vaporisation, J/kg
h_{ref}	refrigerant heat transfer coefficient, W/m^2K
k	thermal conductivity, W/mK
P_i	perimeter of interface, m
P_{iD}	dimensionless perimeter of interface
P_L	perimeter of tube wetted by liquid, m
P_{LD}	dimensionless perimeter of tube wetted by liquid
P_V	perimeter of tube in contact with vapor, m
P_{VD}	dimensionless perimeter of tube in contact with vapor
q	local heat flux, W/m^2
q_{crit}	critical heat flux of nucleate pool boiling, W/m^2
T_{sat}	saturation temperature, K
T_{wall}	wall temperature, K
We_L	liquid Weber number $[G^2D/(\rho_L\sigma)]$
We_V	vapor Weber number $[G^2D/(\rho_V\sigma)]$
x	vapor quality
x_{de}	dryout completion quality
x_{di}	dryout inception quality
x_{IA}	vapor quality at transition from intermittent to annular flow
x_{min}	vapor quality at G_{min}

Greek symbols

ε	cross-sectional vapor void fraction
μ_L	liquid dynamic viscosity, Ns/m^2
μ_V	vapor dynamic viscosity, Ns/m^2
θ_{dry}	dry angle of tube perimeter, rad
θ_{strat}	stratified flow angle of tube perimeter, rad
ρ_L	liquid density, kg/m^3
ρ_V	vapor density, kg/m^3
σ	surface tension, N/m

of the cross-sectional locus of the liquid–vapor interface during stratified-types of flow. For this purpose about 227 000 instantaneous void fractions have been determined using our newly developed optical void fraction measurement system, described in [7]. The frequency of measurements was 50 Hz and the method allowed the void fraction variation as the function of time to be obtained and analysed for different flow conditions in [2].

The second objective of this study was to study the transition from annular to mist flow based on local heat transfer measurements and integrate this boundary into the flow pattern map. Over 1250 new flow boiling heat transfer points have been acquired at mass velocities from 70 to 700 kg/m^2s and heat fluxes from 2.0 to 57.5 kW/m^2 for refrigerants R-22 and R-410A. Local heat transfer coefficients were determined at one position along the liquid heated evaporator, where the wall temperature was measured. The heat flux was derived locally from the heating water enthalpy profile. In Part II, the new mist flow heat transfer data will be presented and new heat transfer prediction methods proposed for the stratified–wavy, dryout and mist flow regimes.

2. State of the art of flow pattern maps

Many flow pattern maps are available for predicting adiabatic two-phase flow regimes in horizontal tubes, such as [8], [9], [10] and Steiner [11]. Very important factors for the flow during evaporation, which have an effect on transition between flow regimes, are nucleate boiling, evaporation of liquid films and acceleration of the flow due to the phase change. It is desirable to define for this type of flow, a flow pattern map that includes the influences of heat flux and dryout on the flow pattern transition boundaries and that is also easy to implement in incremental heat exchanger design schemes.

2.1. Flow pattern map of Kattan–Thome–Favrat

As a first step in this direction, Kattan et al. [1] proposed a modification of the Steiner map, which in turn is a modified Taitel–Dukler map, and which includes a method for predicting the onset of dryout at the top of the tube in diabatic annular flow. This map is presented in coordinates mass velocity versus vapor quality (G vs.

x) that facilitates observation of the evolution of flow pattern transitions at fixed mass velocities with increasing vapor quality along an evaporator tube.

To calculate flow pattern transition curves using their method, the following six dimensionless geometrical variables must first be defined:

$$h_{LD} = \frac{h_L}{D}; \qquad P_{LD} = \frac{P_L}{D} \tag{1}$$

$$P_{VD} = \frac{P_V}{D}; \qquad P_{iD} = \frac{P_i}{D} \tag{2}$$

$$A_{LD} = \frac{A_L}{D^2}; \qquad A_{VD} = \frac{A_V}{D^2} \tag{3}$$

As shown in Fig. 1, D is the internal tube diameter, P_L is the wetted perimeter and P_V is the complementary perimeter in contact with vapor. Similarly, A_L and A_V are the corresponding cross-sectional areas of the liquid and vapor phases, P_i is the length of the phase interface and h_L is the height of the liquid phase from the bottom of the tube.

An iterative method is required to find the above dimensionless variables from the geometrical equations presented in [1]. After calculating them, the flow pattern transition curves can be determined for the defined properties of the fluid. The transition between stratified and stratified–wavy flow will be here designated as "S–SW", between stratified–wavy and intermittent/annular flow as "SW–I/A", between intermittent and annular flow as "I–A", between annular and mist flow as "A–M".

Fig. 2 shows the flow pattern map of Kattan compared to Steiner for R-410A at T_{sat} = 5 °C. The transition curves "SW–I/A" of Kattan (solid lines) are strongly influenced by the effect of onset of dryout compared to the adiabatic curve of Steiner (dashed line). Based on Kattan's flow pattern observations, his curve is also raised by 50 kg/m^{2}s. Regarding the "A–M" transition curve, Kattan added a criterion to avoid the possibility of a mist flow reverting back again to annular flow with increasing vapor quality. Two other transition curves "S–SW" and "I–A" were not modified and are the same as those of Steiner.

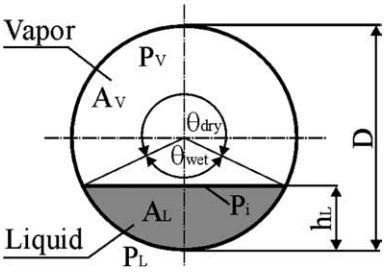

Fig. 1. Stratified two-phase flow cross-section.

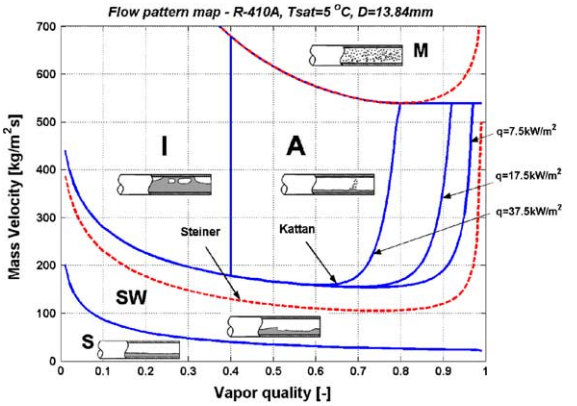

Fig. 2. Flow pattern map of Kattan compared to Steiner for R-410A at T_{sat} = 5 °C in a 13.84 mm internal diameter tube at heat fluxes of 7.5, 17.5 and 37.5 kW/m^2.

Kattan verified his flow pattern map for 702 experimental points for five refrigerants tested over a wide range of pressures, vapor qualities and mass velocities representative of direct-expansion evaporator conditions. These observations showed that 96.2% of the flow pattern data were identified correctly with his diabatic flow pattern map. It must be noted that the "A–M" transition boundary was not investigated experimentally in the work of Kattan. A further 84 observations for R-407C in [12] also showed a 85.7% success rate and the wrong prediction was observed only at the lowest vapor qualities.

2.2. Flow pattern map of Thome and El Hajal

As a practical option and for consistency between the flow map and heat transfer model, an easier to implement version of the map was proposed by Thome and El Hajal [13]. In the previously presented flow pattern map, dimensionless variables A_{LD}, A_{VD}, h_{LD} and P_{iD} were calculated in an iterative way using the stratified flow void fraction model of Taitel–Dukler [9] illustrated in Fig. 1. On the other hand, the flow boiling heat transfer model of Kattan et al. [4] uses the Steiner [11] version of the Rouhani–Axelsson drift flux model for horizontal tubes for the cross-sectional void fraction ε:

$$\varepsilon = \frac{x}{\rho_V}\left[(1+0.12(1-x))\left(\frac{x}{\rho_V}+\frac{1-x}{\rho_L}\right) + \frac{1.18(1-x)[g\sigma(\rho_L-\rho_V)]^{0.25}}{G\rho_L^{0.5}}\right]^{-1} \tag{4}$$

This drift flux void fraction model is easy to apply and gives the void fraction as an explicit function of total mass flux, which the method of Taitel–Dukler does not. Hence, it makes sense to use the same void fraction model in both the flow pattern map and the flow boiling

heat transfer model, for which the Rouhani–Axelson model is a better choice as a general method. This was later proven experimentally by making 238 void fraction measurements for R-22 and R-410A in Wojtan et al. [2] in stratified types of flow.

Then, from the sectional area of the tube A, the values A_{LD} and A_{VD} are directly determinable as:

$$A_{LD} = \frac{A(1-\varepsilon)}{D^2} \tag{5}$$

$$A_{VD} = \frac{A\varepsilon}{D^2} \tag{6}$$

The dimensionless liquid height h_{LD} and the dimensionless length of the liquid interface P_{iD} can be expressed as a function of stratified angle θ_{strat}:

$$h_{LD} = 0.5\left(1 - \cos\left(\frac{2\pi - \theta_{strat}}{2}\right)\right) \tag{7}$$

$$P_{iD} = \sin\left(\frac{2\pi - \theta_{strat}}{2}\right) \tag{8}$$

To avoid completely any iteration, the geometrical expression for the stratified angle θ_{strat} can be calculated from an approximate expression, evaluated in terms of void fraction, by Biberg [14] as follows:

$$\theta_{strat} = 2\pi - 2\left\{\begin{array}{l}\pi(1-\varepsilon) + \left(\frac{3\pi}{2}\right)^{1/3}[1-2(1-\varepsilon)+(1-\varepsilon)^{1/3}-\varepsilon^{1/3}] \\ -\frac{1}{200}(1-\varepsilon)\varepsilon[1-2(1-\varepsilon)][1+4((1-\varepsilon)^2+\varepsilon^2)]\end{array}\right\} \tag{9}$$

As the void fraction is a function of mass velocity, in the Thome–El Hajal map it influences the position of the transition curves. The minor effect of mass velocity on flow regime transitions is shown in Fig. 3. The strongest effect of mass velocity is observed for the "SW–I/A" transition curve for vapor qualities below 0.1, where the transition curve goes up with increasing mass velocity. This divergence becomes less significant as the vapor quality increases. The boundary curve "A–M" also moves up marginally with increasing mass velocity.

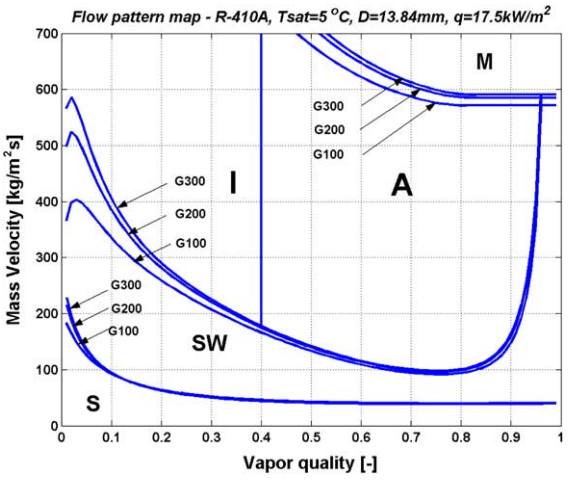

Fig. 3. Flow pattern map of Thome–El Hajal for R-410A at $T_{sat} = 5\,^{\circ}C$ in a 13.84 mm internal diameter tube with its equations evaluated at three fixed mass velocities: $G = 100$, 200 and 300 kg/m^{2}s.

3. Flow boiling test facility with optical void fraction measurement system

Fig. 4 shows a simplified layout of the LTCM intube refrigerant test loop with a close up view of the set-up used for the dynamic void fraction measurements. The refrigerant first passes through a series of horizontal electrical preheaters and then through an insulated tube without any sharp elbows. Then, the refrigerant enters the tubular test section and is heated by counter-current flow of hot water in the annulus of the double pipe system. The inlet refrigerant vapor quality is regulated by the heating power of the preheater. The void fraction is measured at the outlet of the test section as shown and the refrigerant then goes through a condenser, a magnetically driven gear pump (oil free) and finally, a Coriolis mass flow meter. The circuit also includes a vapor–liquid reservoir for controlling the amount of refrigerant in the circuit and thus the operating pressure. The hot water flow rate in the annulus is measured with another calibrated Coriolis mass flow meter.

As shown in Fig. 5, a CCD camera is situated above the glass observation tube and records the illuminated laser sheet images of the liquid–vapor interface in the cross-section of the tube. The images are distorted by the double refraction of the light through the glass and by the variation in magnification of the image by the oblique orientation of the camera. Based on the deformation of a regular grid placed inside the glass tube during preliminary tests, the images are transformed to their orthogonal view and the interface between gas and liquid is found. Then the void fraction is determined by the calculation of the ratio of the number of pixels corresponding to the vapor phase and the total pixels corresponding to the total cross-sectional area of the tube. The image acquisition rate was 25 frames per second. Because of the interlaced acquisition mode (i.e. even lines and odd lines are not recorded at the same time), a resampling procedure was performed. The resampling technique yields two images from the interlaced one and thus increases the acquisition rate to 50 frames per second. The calibration method shows that the absolute error of the new void fraction measurement system does not exceed ±0.01 over the entire range of void fractions measurable from about 0.02 to 0.95 for stratified types of flow. The optical void fraction measurement technique with the image processing system is described in Ursenbacher et al. [7].

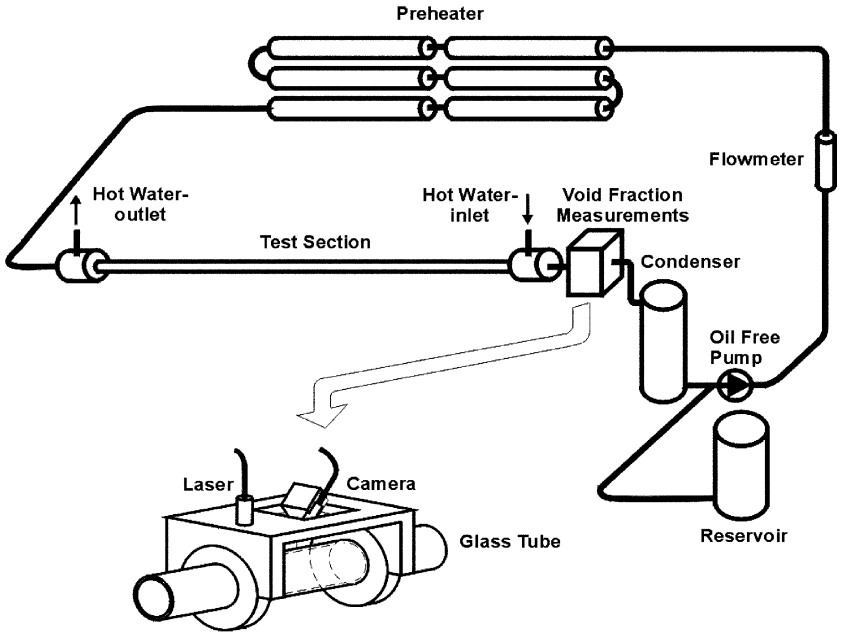

Fig. 4. Flow boiling test facility with the void fraction measurement system.

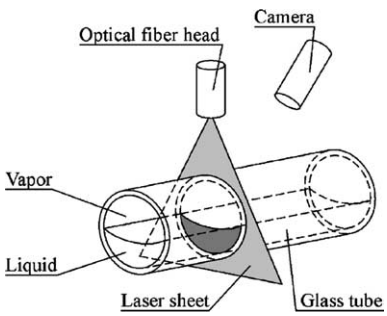

Fig. 5. Schematic of the optical set-up.

The temperature of the hot water is measured at five positions (using 26 thermocouples) that allows the enthalpy profile along the test section to be determined and from that the local heat flux q. The temperature of the refrigerant T_{sat} is determined by the measurement of the saturation pressure at the inlet and outlet of the test section (assuming a linear variation). The wall temperature T_{wall} is measured using four thermocouples installed on the external wall of the tested tube (taking the mean of the measurements at the top, two sides and bottom of the tube wall). Then, the refrigerant local heat transfer coefficient was calculated as follows:

$$\frac{1}{h_{ref}} = \frac{T_{wall} - T_{sat}}{q} - \frac{\ln(D_{ext}/D)D}{2k} \tag{10}$$

where D_{ext} and D are the external and internal diameters of the copper tube and k is the thermal conductivity of copper.

More technical details concerning the test section and the heat transfer measurements are presented in Part II of this paper.

4. Development of the new version of the flow pattern map

The flow pattern oriented heat transfer model of Kattan et al. [4] was developed for vapor qualities higher than 0.15. According to the flow pattern map presented in Fig. 6, all points less than the vapor quality of 0.15 and below the G_{wavy} curve are identified as stratified–wavy and for the lowest mass velocities (below G_{strat}) as stratified flow. Kattan [3] suggested that the frequency of waves in this region is very influential on the local heat transfer coefficient. He proposed in the future to divide this zone into two subzones according to an all wet or partially wet criterion. Zürcher [16] found also that the flow pattern oriented model of Kattan et al. did not work as well for stratified–wavy flows as for annular ones.

In this light the dynamic void fraction results from [2] will be used to discern the transitions between the respective flow regimes in stratified types of flow. The optical void fraction measurements technique is applicable only for stratified, stratified–wavy and slug flows. In the present tests, the slug and wave slopes were nearly never higher than the inclination angle of the camera, which would block the camera's view of the interface. It allowed using the optical transformation developed for the static conditions taking into account only light

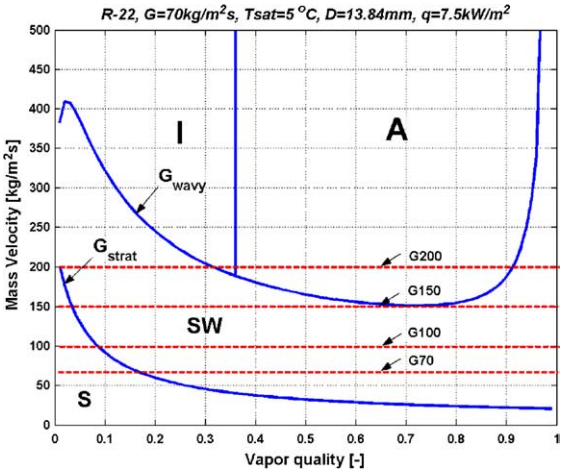

Fig. 6. Flow pattern map of Thome–El Hajal for R-22 at $T_{sat} = 5$ °C in the 13.84 mm test section (graph was prepared assuming a fixed value of $G = 70$ kg/m^{2}s).

refraction through the glass. In annular flow, the light is refracted through the glass as well as through the upper liquid film and the optical transformation developed for stratified types of flows is no more valid. Since void fraction measurements were not feasible in annular flow, the investigation of the transition to mist flow uses the measured acute variations of the local heat transfer coefficients as a function of vapor quality for identifying these transitions.

4.1. Modification in the stratified–wavy region

4.1.1. Experimental conditions of void fraction measurements

As described in Wojtan et al. [2], dynamic void fractions were measured for R-22 at mass velocity conditions of 70, 100, 150 and 200 kg/m^{2}s (see Fig. 6 for the expected regimes) and R-410A for 70, 150, 200 and 300 kg/m^{2}s. The internal diameter of the tested sight glass tube was 13.6 mm (nearly identical to that of the heat transfer test section of 13.84 mm). The saturation temperature T_{sat} was 5 °C and the heat fluxes in the heat transfer section ranged from 2.0 to 7.5 kW/m^2 (low heat fluxes were used to avoid nucleate boiling and its entrained bubbles in the flow). After reaching a steady-state condition, the cross-sectional image sequences were simultaneously acquired with all the heat transfer parameters. At each mass velocity, these acquisitions were repeated for 25–37 different vapor qualities. For each case, the acquisition time was between 18 and 20 seconds and provided 900–1000 images, that were then processed to obtain a time-averaged void fraction value at each test condition. All together, 238 time-averaged experimental void fraction points have been acquired corresponding to about 227 000 images in Wojtan et al. [2]. In this study, our focus will be on the variation of the void fraction as a function of time as a means to identify the characteristics of the flow.

4.1.2. Results of dynamic void fraction measurements

As can be seen in Fig. 6 at the mass velocity $G = 70$ kg/m^{2}s, the flow pattern map predicts stratified flow at vapor qualities below 0.15 and stratified–wavy flow above. At the higher mass velocity of $G = 200$ kg/m^{2}s, stratified–wavy flow is predicted in the vapor quality range from 0 to 0.30 and in the partial dryout region at high vapor qualities. For these two mass velocities some experimental data will be discussed in detail below.

Fig. 7(a)–(d) shows experimental results of instantaneous void fractions as a function of time for R-22 tested at $G = 70$ kg/m^{2}s and vapor qualities of 0.044, 0.115, 0.154 and 0.327, respectively. For the test at $x = 0.044$, two different flow structures can be distinguish. The first one is a long wave lasting almost 4 seconds and the second is a series of short vapor slugs appearing for the next 8 seconds (each lasting about 1 second). This was then again followed by another long wave lasting about 4 seconds, and so forth. Increasing the vapor quality to $x = 0.115$, the vapor slug duration becomes longer and quite regular (each vapor slug lasts about 2 seconds while the liquid slugs in between are of very short duration and indicated when $\varepsilon = 0$). Further increasing vapor quality to $x = 0.154$ results in fewer vapor slugs with large waves becoming more dominant, while the fluctuations of void fraction are lower and only a few liquid slugs are observed in the test period of 18 seconds (distinguish by void fraction going to zero). At the last vapor quality of $x = 0.327$, fully developed stratified–wavy flow appears, which is characterised by small scale fluctuations in the cross-sectional void fraction by interfacial waves generated by the vapor shear on the stratified liquid. This was observed in other void fraction sequences up to nearly complete evaporation ($x \to 0.95$) at the test mass velocity of $G = 70$ kg/m^{2}s.

Fig. 8(a)–(d) shows experimental results of void fraction as a function of time for R-22 at $G = 200$ kg/m^{2}s and four vapor qualities: 0.054, 0.116, 0.156 and 0.305, respectively. As can be seen in Fig. 8(a)–(c), the frequency of liquid slugs systematically increases. The frequency of liquid slugs can be clearly distinguished and there are no long wave structures between the liquid slugs as detected in the tests at lower mass velocities. At the vapor quality $x = 0.305$, liquid slugs become irregular, void fraction increases and the high velocity vapor starts forming the liquid film around the tube perimeter.

The following conclusions can be drawn from the video observations and void fraction measurements and our other similar results:

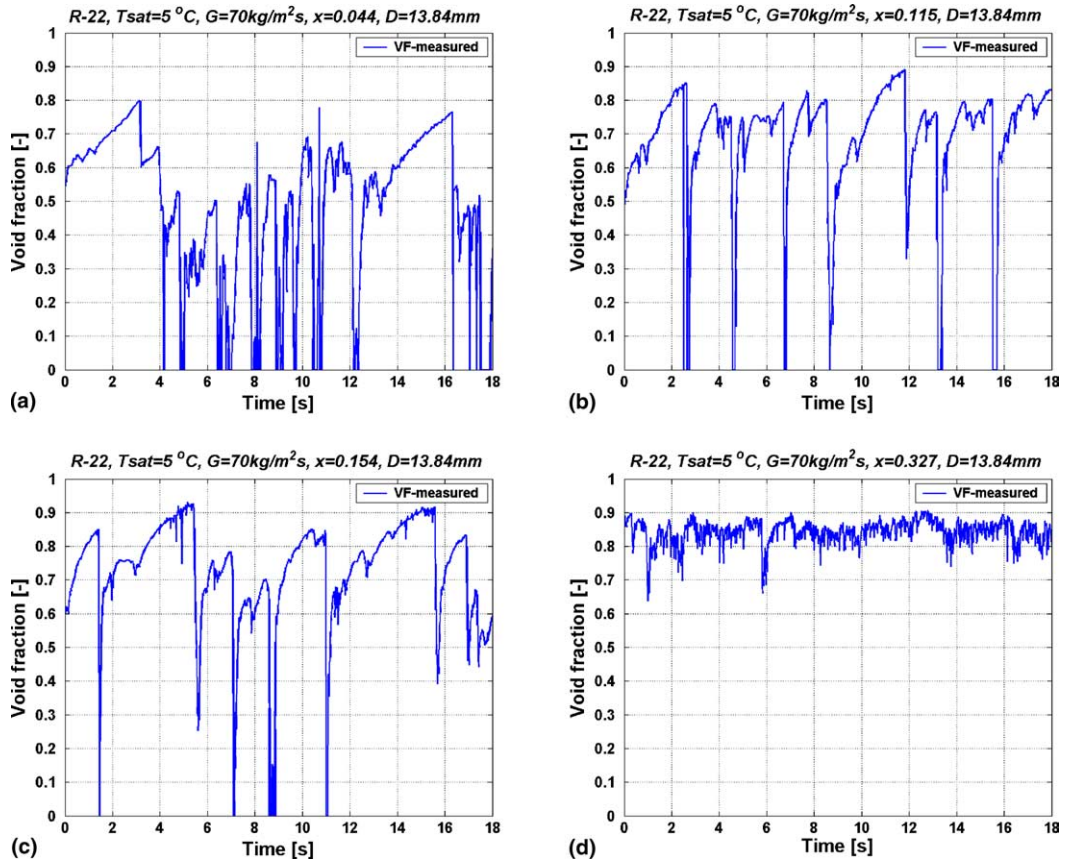

Fig. 7. Void fraction as a function of time for R-22 at $G = 70$ kg/m^{2}s, $T_{sat} = 5$ °C and $D = 13.60$ mm at four vapor qualities: (a) 0.044, (b) 0.115, (c) 0.154, (d) 0.327.

1. Stratified flow was not detected at any of the mass velocities tested.
2. In the vapor quality range $0 < x < x_{IA}$, a mixed flow structure of liquid slugs and stratified–wavy interfaces was observed (x_{IA} is the vertical line separating intermittent and annular flows).
3. The transition from slug/stratified–wavy flows to fully stratified–wavy flows without any slugs appears approximately to occur at x_{IA}.
4. Only slug flow was observed for the zone identified by the Thome–El Hajal map to be in the stratified–wavy region for $G > G_{wavy}(x_{IA})$.

Based on these observations, the stratified–wavy flow region of the Thome–El Hajal version of the flow map has been modified as follows:

1. A new transition line is added at $G_{strat} = G_{strat}(x_{IA})$ at $x < x_{IA}$ (this creates a new horizontal transition line to the left of x_{IA} and modifies the boundary of the stratified (S) regime).
2. The stratified–wavy region has been divided into three subzones:
   - For $G > G_{wavy}(x_{IA})$, this becomes the SLUG zone.
   - For $G_{strat} < G < G_{wavy}(x_{IA})$ and $x < x_{IA}$, this becomes the SLUG/ STRATIFIED-WAVY zone.
   - For $x \geqslant x_{IA}$, this remains as the STRATIFIED-WAVY zone.

Fig. 9 depicts the new flow pattern map for R-22 at $T_{sat} = 5$ °C in the 13.84 mm test section, evaluated at $G = 100$ kg/m^{2}s and $q = 2.1$ kW/m^2 with the above modifications applied to the Thome–El Hajal version of Kattan–Thome–Favrat flow pattern map to better describe the actual character of the flow. The dash-pointed lines correspond to the new dryout and mist flow transitions curves described in the next section.

4.2. New transition curves in post dryout regime

4.2.1. Experimental conditions of heat transfer measurements

Over 1250 new experimental heat transfer points were measured for R-22 and R-410A at mass velocities from 70 to 700 kg/m^{2}s and heat fluxes from 2.0 to

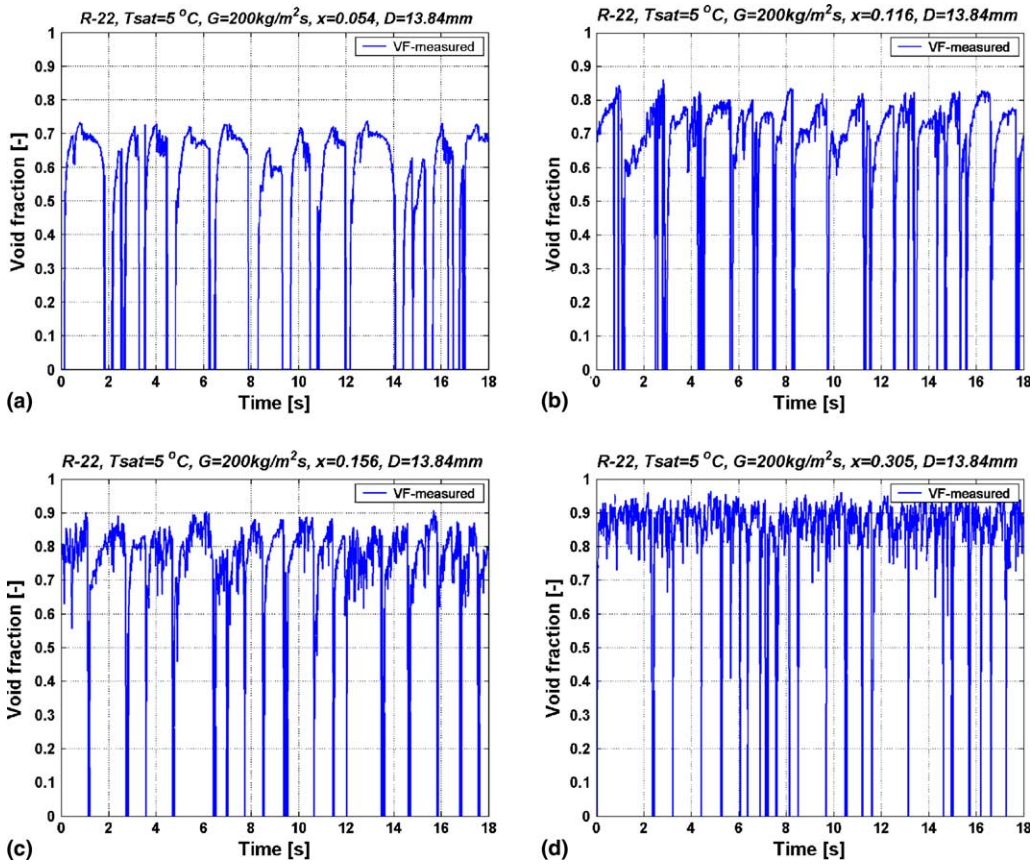

Fig. 8. Void fraction as a function of time for R-22 at $G = 200$ kg/m^{2}s, $T_{sat} = 5$ °C and $D = 13.60$ mm at four vapor qualities: (a) 0.054, (b) 0.116, (c) 0.156, (d) 0.305.

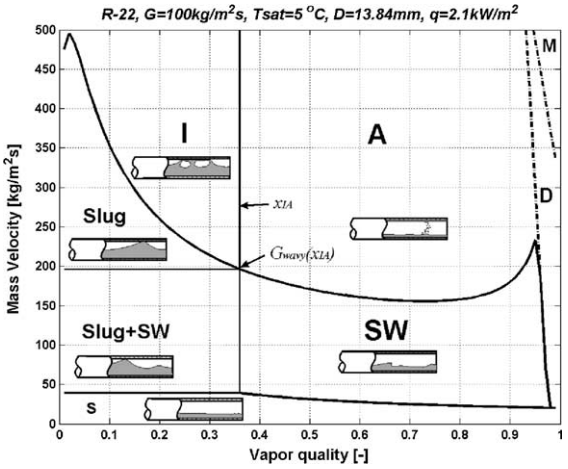

Fig. 9. New flow pattern map for R-22 at $T_{sat} = 5$ °C in the 13.84 mm test section at $G = 100$ kg/m^{2}s and $q = 2.1$ kW/m^2.

57.5 kW/m^2, of which 368 experimental points were measured in partial dryout and mist flow conditions. The tube internal diameters tested were 13.84 mm for R-22 and R-410A as well as 8.00 mm for R-410A.

Fig. 10 illustrates five sets of data (solid points) obtained for R-22. The rapid decrease of the heat transfer coefficient with increasing vapor quality indicates the inception of dryout. The end of this decrease of heat transfer coefficient marks the end of dryout and the beginning of mist flow. Heat transfer coefficients obtained at mass velocities ranging from 300 to 700 kg/m^{2}s and at initial heat fluxes from 7.5 to 57.5 kW/m^2 will be used here to find the annular to dryout "A–D" and dryout to mist "D–M" transition curves. The observations in the sight glass confirmed that the dryout and mist flow appeared at the same vapor quality as detected by the heat transfer measurements.

4.2.2. Results of heat transfer measurements

Fig. 11(a) and (b) shows the post dryout heat fluxes in the 13.84 mm test section for R-22 and R-410A, respectively. The initial heat fluxes were $q = 37.5$ kW/m^2 and $q = 57.5$ kW/m^2. An initial heat flux refers to the heat flux measured before the onset of dryout occurs

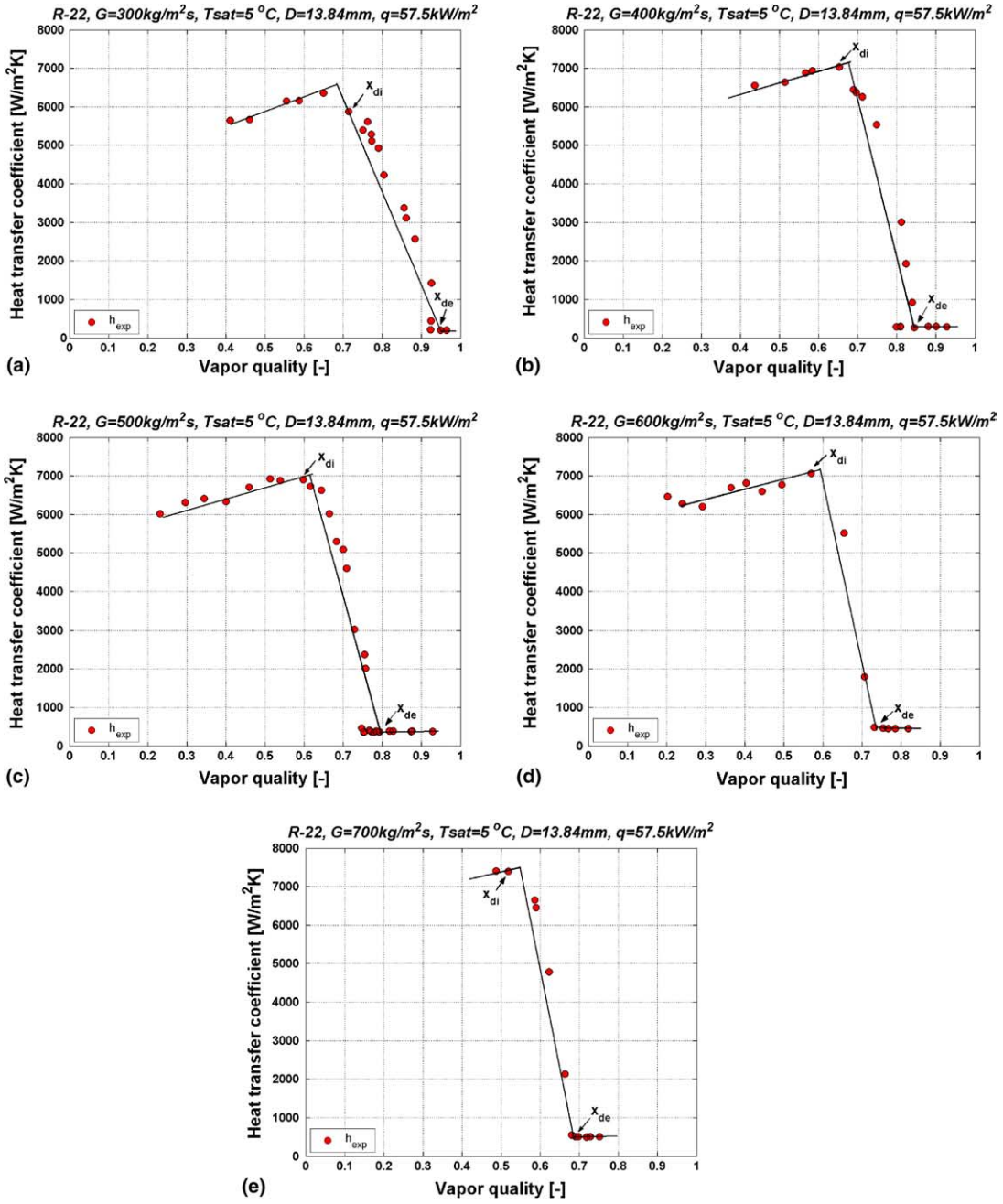

Fig. 10. Experimental heat transfer coefficients in the 13.84 mm test section for R-22 at T_{sat} = 5 °C with an initial heat flux q = 57.5 kW/m^2 at five mass velocities: (a) 300 kg/m^{2}s, (b) 400 kg/m^{2}s, (c) 500 kg/m^{2}s; (d) 600 kg/m^{2}s, (e) 700 kg/m^{2}s.

(prior to dryout). As can be seen for the initial heat flux q = 37.5 kW/m^2, the post dryout heat flux varies between 4.3 and 7.4 kW/m^2 for R-22 and 5.4–7.7 kW/m^2 for R-410A. For the initial heat flux q = 57.5 kW/m^2, the post dryout heat flux varies in the range 5.2–12.2 kW/m^2 for R-22 and 8.4–15.2 kW/m^2 for R-410A. The decrease of the heat flux from the initial value varies between 74% and 91% and is lower as the mass velocity increases.

The big drop in the heat flux results in a corresponding rapid decrease in the heat transfer coefficient relative to that prior to dryout. The heat transfer coefficient falls over a limited quality range and then becomes nearly constant in value as seen in Fig. 10. This variation is also

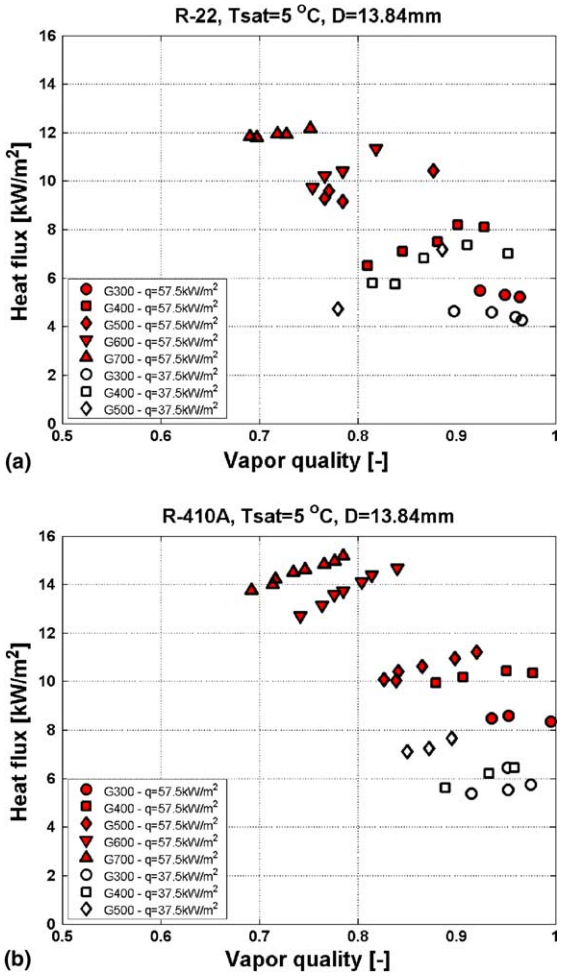

Fig. 11. Post dryout heat flux evolution for initial condition $q = 37\ \mathrm{kW/m^2}$ and $q = 57\ \mathrm{kW/m^2}$ in the 13.84 mm test section for (a) R-22 and (b) R-410A.

shown in Fig. 12 and has been traced by Mori et al. [15] by three straight lines.

The point of intersection B indicates the inception point of dryout at the top of the horizontal tube, where locally the heat transfer begins to fall as the annular film dries out. The point of intersection C indicates the location where dryout is complete around the tube perimeter, and thus also where the deterioration of the heat transfer ends. The qualities at the respective points are denoted x_{di} and x_{de}. The distinction of these two points is caused by the shift of the dryout position from the top to the bottom around and along the tube perimeter with increasing quality and also by the irregular fluctuations of the axial dryout position due to the unstable nature of the process as per Mori et al. [15]. Similar trends were clearly observed during the present evaporation tests.

As mentioned before, Fig. 10(a)–(e) shows experimental results for the local heat transfer coefficient mea-

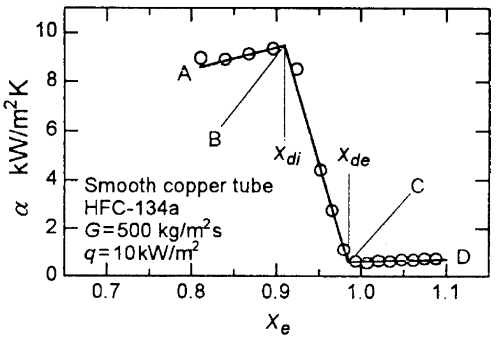

Fig. 12. Approximation of heat transfer coefficient in the neighborhood of dryout from Mori et al. [15].

surements in the 13.84 mm test section for R-22 at the initial heat flux $q = 57.5\ \mathrm{kW/m^2}$ at mass velocities of 300, 400, 500, 600 and 700 $\mathrm{kg/m^2 s}$, respectively. Like in the approach of Mori et al. [15], the variation of heat transfer can be traced by the three straight lines. In annular flow close to dryout inception, the heat transfer coefficient increases with increasing vapor quality almost linearly. The dryout inception quality x_{di} is determined in this study as the last point before the heat flux dropped more than by 10% from its initial value. The dryout completion quality x_{de} was determined as the first datapoint within the plateau of the mist flow results. There is some hysteresis in the process when reducing the heat duty after reaching mist flow, as indicated by the stable data points at vapor qualities just below x_{de}. In the dryout transition zone (between annular and mist flow), the heat transfer coefficient can be modelled by a steep line, which intersects the nearly horizontal line representing mist flow heat transfer. The experimental point at which the decline of heat transfer coefficient ends is considered to be the end of dryout and is denoted as x_{de}. It is observed that the dryout inception x_{di} appears at lower vapor qualities as the mass velocity increases. For example, for the initial heat flux $q = 57.5\ \mathrm{kW/m^2}$, x_{di} varies between 0.52 and 0.72 at the mass velocities $G = 700\ \mathrm{kg/m^2 s}$ and $G = 300\ \mathrm{kg/m^2 s}$, respectively. For the same conditions, the end of dryout x_{de} varies between 0.68 and 0.92.

Performing the same procedure, the dryout inceptions x_{di} and dryout completions x_{de} qualities have been found for all test conditions. The results for the tests in the 13.84 mm internal diameter tube with R-22 and R-410 A are presented in Fig. 13(a) and (b), respectively. Fig. 13(c) shows x_{di} and x_{de} obtained in the tests with R-410A in the 8.00 mm *ID* test section.

Comparing the dryout inceptions for both fluids, it can be seen that x_{di} appears at much lower vapor qualities for R-410 A than for R-22. This could be explained as the effect of surface tension, which is by almost 30% lower for R-410A compared to R-22.

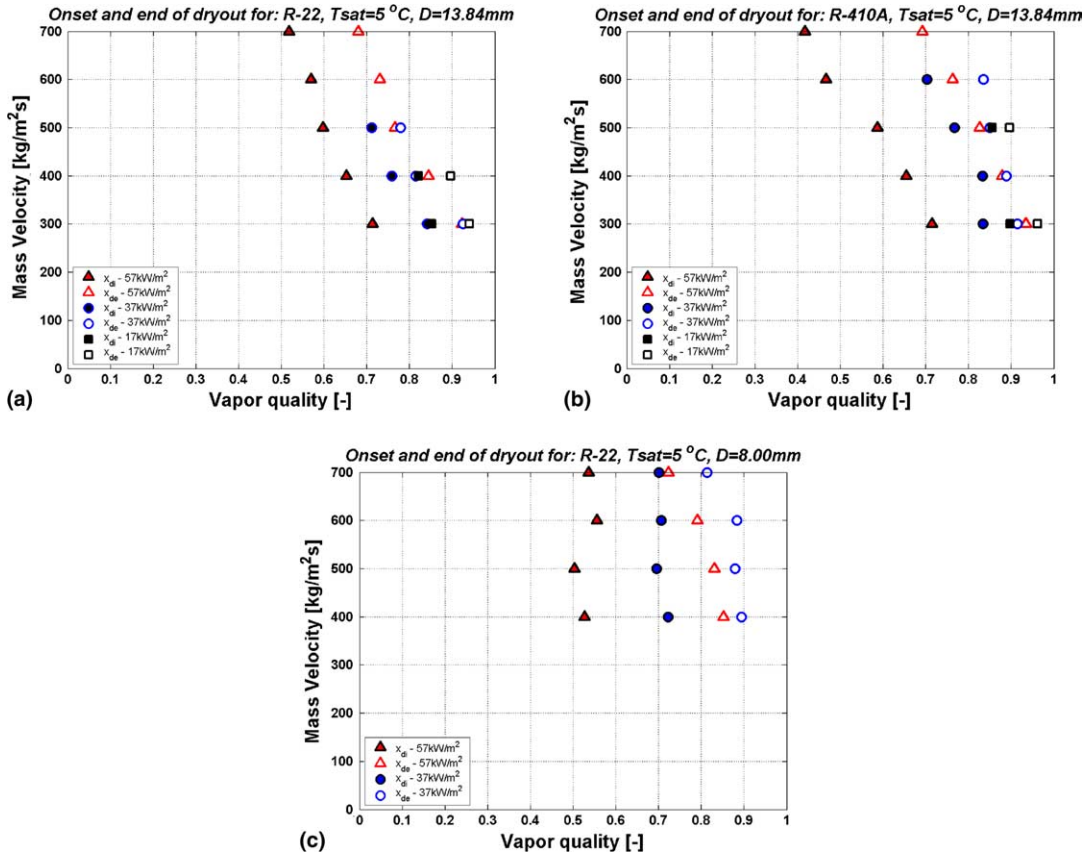

Fig. 13. The dryout inception x_{di} and the dryout completion x_{de} for: (a) R-22, D = 13.84 mm; (b) R-410A, D = 13.84 mm; (c) R-410A, D = 8.00 mm.

As the surface tension decreases, it is easier to entrain the liquid film into the high velocity vapor core and the dryout inception is encountered at lower quality.

Analysing experimental results and observations in the sight glass, it is obvious that there is no step-wise transition from annular flow to mist flow. As depicted in Fig. 14, dryout occurs at the top of the tube first (cross section A–A), where the liquid film is thinner, and then progresses downward around the perimeter (cross section B–B) until reaching the bottom (cross section C–C). The process of dryout thus takes place over a range of vapor qualities and ends at the bottom of the tube when the fully developed mist flow regime is reached. This regime between x_{di} and x_{de} will be called dryout.

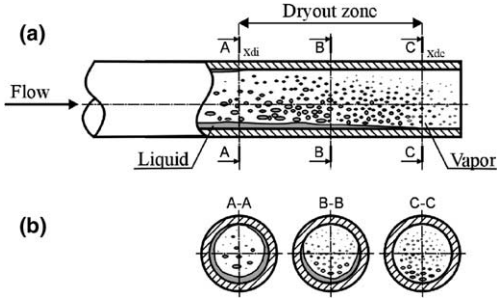

Fig. 14. (a) Dryout zone during evaporation in a horizontal tube; (b) Cross sections: A–A onset of dryout in annular flow; B–B dryout; C–C end of dryout and beginning of mist flow.

The first attempt to model the annular–dryout transition during evaporation in horizontal tubes was made by Lavin and Young [16]. They proposed a new transition between the annular and dryout zones based on the Weber number for R-22 and R-12. Lavin and Young observed the dryout process, but with the apparatus used, they could not obtain the heat transfer coefficient within the dryout regime nor study the conditions under which the dryout regime ends and stable mist flow was established.

Kattan et al. (see Section 2.1) used the Steiner version of the Taitel–Dukler "A–M" curve to predict the transition from annular to mist flow. He added a criterion to avoid the possibility of a mist flow reverting back again to annular flow with increasing vapor quality. This approach does not distinguish between annular–dryout

"A–D" and dryout–mist flow "D–M" transitions and predicts the annular–mist flow transition only by one curve, which in horizontal *diabatic* flow is not appropriate as shown above. It has to be noted that this transition boundary was not investigated experimentally in the work of Kattan.

Since dryout proceeds over an interval of vapor quality, Mori et al. [15] defined dryout inception x_{di} and dryout completion x_{de} using three characteristic regimes: *S1*, *S2* and *S3*. The best agreement of our experimental data has been found with their dryout inception x_{di} and dryout completion x_{de} defined for the regime *S2* of the form:

$$x_{di} = 0.58e^{[0.52-2.1\cdot10^{-5}We_V^{0.96}Fr_V^{-0.02}(\rho_V/\rho_L)^{-0.08}]} \quad (11)$$

$$x_{de} = 0.61e^{[0.57-2.65\cdot10^{-5}We_V^{0.94}Fr_V^{-0.02}(\rho_V/\rho_L)^{-0.08}]} \quad (12)$$

The approach of Mori et al. has been extended here by including the heat flux effect using the non-dimensional ratio (q/q_{crit}) and new empirical factors have been found based on all experimental points and using the least square error method. Thus, the new limits of dryout can be calculated from the following equations:

$$x_{di} = 0.58e^{[0.52-0.235\cdot We_V^{0.17}Fr_V^{0.37}(\rho_V/\rho_L)^{0.25}(q/q_{crit})^{0.70}]} \quad (13)$$

$$x_{de} = 0.61e^{[0.57-5.8\cdot10^{-3}We_V^{0.38}Fr_V^{0.15}(\rho_V/\rho_L)^{-0.09}(q/q_{crit})^{0.27}]} \quad (14)$$

where the critical heat flux q_{crit} is used to nondimensionalize the expression, calculated with that of Kutateladze [17] as:

$$q_{crit} = 0.131\rho_V^{0.5}h_{LV}(g(\rho_L-\rho_V)\sigma)^{0.25} \quad (15)$$

After inversion of the above equations to mass velocity as a function of vapor quality, the transitions curves "A–D" and "D–M" become respectively:

$$G_{dryout} = \left[\frac{1}{0.235}\left(\ln\left(\frac{0.58}{x}\right)+0.52\right)\left(\frac{D}{\rho_V\sigma}\right)^{-0.17} \times \left(\frac{1}{gD\rho_V(\rho_L-\rho_V)}\right)^{-0.37}\left(\frac{\rho_V}{\rho_L}\right)^{-0.25}\left(\frac{q}{q_{crit}}\right)^{-0.70}\right]^{0.926} \quad (16)$$

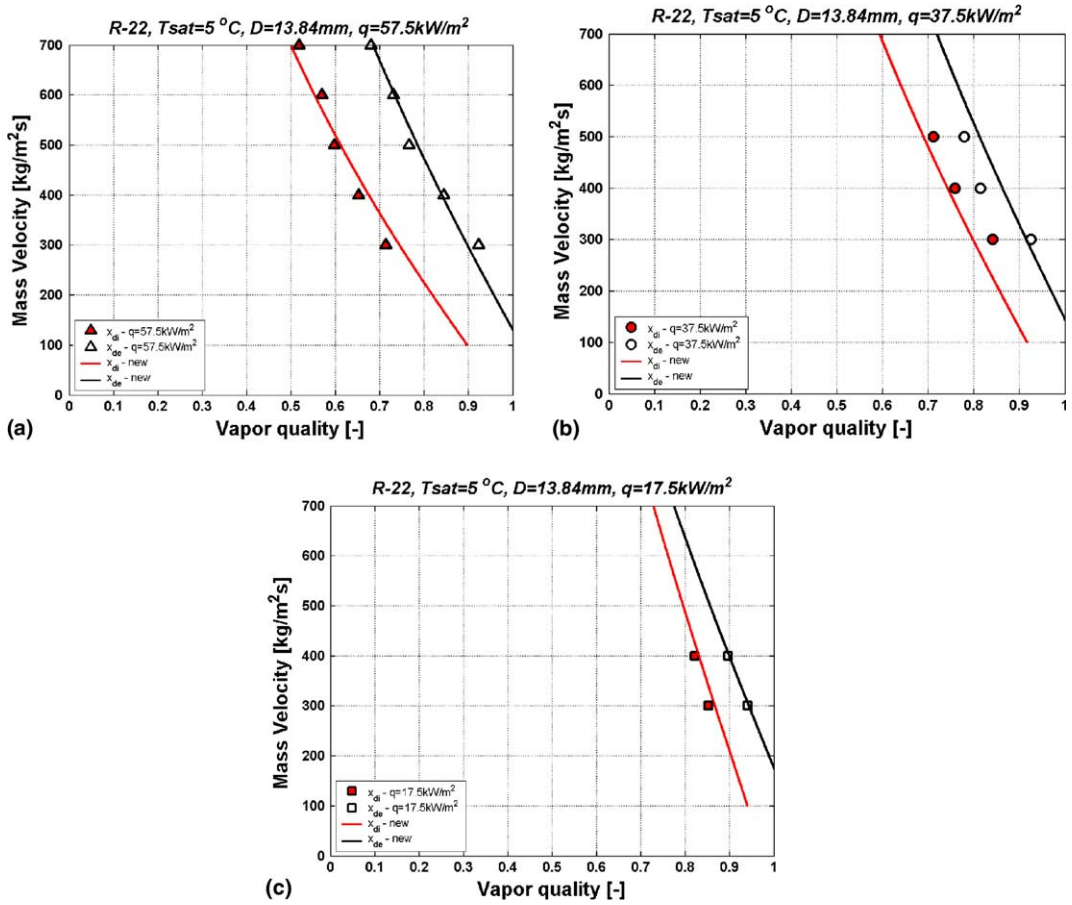

Fig. 15. New transition curves for the annular–dryout and dryout–mist flow experimental results of R-22 in the 13.84 mm test section at three initial heat fluxes: (a) 57.5 kW/m^2, (b) 37.5 kW/m^2, (c) 17.5 kW/m^2.

$$G_{\text{mist}} = \left[\frac{1}{0.0058}\left(\ln\left(\frac{0.61}{x}\right)+0.57\right)\left(\frac{D}{\rho_V\sigma}\right)^{-0.38} \times \left(\frac{1}{gD\rho_V(\rho_L-\rho_V)}\right)^{-0.15}\left(\frac{\rho_V}{\rho_L}\right)^{0.09}\left(\frac{q}{q_{\text{crit}}}\right)^{-0.27}\right]^{0.943} \quad (17)$$

Fig. 15 shows the new transition curves calculated from Eqs. (16) and (17) compared to x_{di} and x_{de} obtained during evaporation tests with R-22 in the 13.84 mm test section. As can be seen, very good agreement has been found between the prediction and experimental points for all three initial heat fluxes. Similar results have been obtained for the evaporation tests with R-410A and the smaller tube.

4.3. Implementation of the new flow pattern map

Taking into account the above modification in the stratified–wavy region and integrating the new "A–D" and "D–M" transitions curves, the implementation procedure is as follows:

1. Geometrical parameters ε, A_{LD}, A_{VD}, θ_{strat}, h_{LD} and P_{id} are calculated from Eqs. (4)–(6), (9), (7) and (8), respectively.
2. As the effect of heat flux at high vapor quality is captured by the "*A–D*" and "*D–M*" transition curves, the "*SW–I/A*" transition is first calculated from the following adiabatic version of the original Kattan–Thome–Favrat [1] boundary:

$$G_{\text{wavy}} = \left\{\frac{16A_{\text{VD}}^3 gD\rho_L\rho_V}{x^2\pi^2(1-(2h_{\text{LD}}-1)^2)^{0.5}} \times \left[\frac{\pi^2}{25h_{\text{LD}}^2}\cdot\left(\frac{We}{Fr}\right)_L^{-1}+1\right]\right\}^{0.5}+50 \quad (18)$$

The stratified–wavy region is then subdivided into three zones:

- $G > G_{\text{wavy}}(x_{\text{IA}})$ gives the SLUG zone;
- $G_{\text{strat}} < G < G_{\text{wavy}}(x_{\text{IA}})$ and $x < x_{\text{IA}}$ give the SLUG/STRATIFIED-WAVY zone;
- $x \geqslant x_{\text{IA}}$ gives the STRATIFIED-WAVY zone.

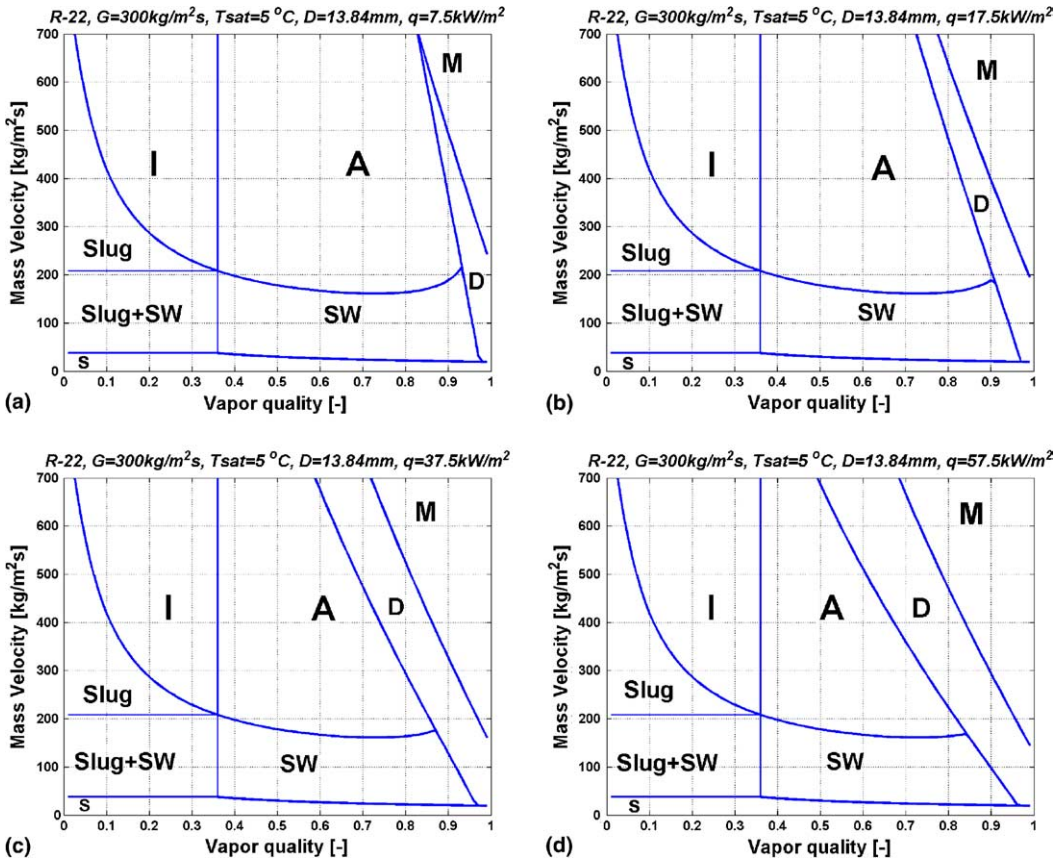

Fig. 16. New flow pattern maps for R-22 at T_{sat} = 5 °C and D = 13.84 mm at G = 300 kg/m^{2}s and four initial heat fluxes: (a) 7.5 kW/m^2, (b) 17.5 kW/m^2, (c) 37.5 kW/m^2, (d) 57.5 kW/m^2.

3. The "*S–SW*" transition is calculated from the original Kattan–Thome–Favrat [1] boundary:

$$G_{\text{strat}} = \left\{ \frac{226.3^2 A_{\text{LD}} A_{\text{VD}}^2 \rho_{\text{V}} (\rho_{\text{L}} - \rho_{\text{V}}) \mu_{\text{L}} g}{x^2 (1-x) \pi^3} \right\}^{1/3} \tag{19}$$

but now $G_{\text{strat}} = G_{\text{strat}}(x_{\text{IA}})$ at $x < x_{\text{IA}}$.

4. The "*I–A*" transition is calculated from the original Kattan–Thome–Favrat [1] boundary:

$$x_{\text{IA}} = \left\{ \left[0.34^{1/0.875} \left(\frac{\rho_{\text{V}}}{\rho_{\text{L}}} \right)^{-1/1.75} \left(\frac{\mu_{\text{L}}}{\mu_{\text{V}}} \right)^{-1/7} \right] + 1 \right\}^{-1} \tag{20}$$

and extended down to its intersection with G_{strat}.

5. The "*A–D*" boundary is calculated from Eq. (16).
6. The "*D–M*" boundary is calculated from Eq. (17).
7. The following conditions are then applied to define the transitions in the high vapor quality range:
   (i) If $G_{\text{strat}}(x_{\text{i}}) \geqslant G_{\text{dryout}}(x_{\text{i}})$, then $G_{\text{dryout}}(x_{\text{i}}) = G_{\text{strat}}(x_{\text{i}})$
   (ii) If $G_{\text{wavy}}(x_{\text{i}}) \geqslant G_{\text{dryout}}(x_{\text{i}})$, then $G_{\text{dryout}}(x_{\text{i}}) = G_{\text{wavy}}(x_{\text{i}})$
   (iii) If $G_{\text{dry}}(x_{\text{i}}) \geqslant G_{\text{mist}}(x_{\text{i}})$ (possible at low heat fluxes and high mass velocities) than $G_{\text{dry}}(x_{\text{i}}) = G_{\text{mist}}(x_{\text{i}})$

where x_{i} is the considered vapor quality.

Fig. 16(a)–(d) shows the new flow pattern map for R-22 at $T_{\text{sat}} = 5$ °C, $D = 13.84$ mm and heat fluxes of 7.5, 17.5, 37.5 and 57.5 kW/m^2, respectively. Compared to the Kattan–Thome–Favrat map, the new regimes: slug (Slug), slug/stratified–wavy (Slug + SW) and dryout (*D*) are now encountered. Notably, it is observed that the dryout and mist flow regions become smaller as the value of the initial heat flux decreases.

5. Conclusions

New transition curves have been found to define annular–dryout and dryout–mist flow transitions based on our new heat transfer measurements and observations. The curves have been integrated into the Thome–El Hajal version of the Kattan–Thome–Favrat flow pattern map. Based on measurements and trends observed in the dynamic void fraction, the stratified–wavy region has been subdivided into three zones: slug, slug/stratified–wavy and stratified–wavy. Furthermore, the transition curve stratified/stratified–wavy flow has been adjusted for vapor qualities below x_{IA}. These modifications provide a more accurate prediction of the flow regimes below G_{wavy} and significantly improve the identification the inception of dryout. All procedures to calculate the new flow pattern map have been presented. The new flow pattern map does not require any iterative calculations and it can be easily used for flow regime identification in the flow boiling heat transfer model.

Acknowledgement

These investigations are supported by the Swiss National Fund (FNS) contract number 21-57210.99 and by the Air-Conditioning and Refrigeration Technology Institute (ARTI) contract number 605-20040.

References

[1] N. Kattan, J.R. Thome, D. Favrat, Flow boiling in horizontal tubes. Part 1: Development of a diabatic two-phase flow pattern map, J. Heat Transfer 120 (1) (1998) 140–147.
[2] L. Wojtan, T. Ursenbacher, J.R. Thome, Dynamic void fractions in stratified types of flow, Part II: Measurements for R-22 and R-410A, Int. J. Multiphase Flow 30 (2004) 125–137.
[3] N. Kattan, Contribution to the heat transfer analysis of substitute refrigerants in evaporator tubes with smooth or enhanced tube surfaces, PhD thesis, Dept. of Mechanical Engineering, Swiss Federal Institute of Technology Lausanne, CH-1015 Lausanne, Switzerland, 1996.
[4] N. Kattan, J.R. Thome, D. Favrat, Flow boiling in horizontal tubes. Part 3: Development of a new heat transfer model based on flow patterns, J. Heat Transfer 120 (1) (1998) 156–165.
[5] J. El Hajal, J.R. Thome, A. Cavallini, Condensation in horizontal tubes, part 1: Two-phase flow pattern map, Int. J. Heat Mass Transfer 46 (18) (2003) 3349–3363.
[6] J. El Hajal, J.R. Thome, A. Cavallini, Condensation in horizontal tubes, Part 2: New heat transfer model based on flow regimes, Int. J. Heat Mass Transfer 46 (18) (2003) 3365–3387.
[7] T. Ursenbacher, L. Wojtan, J.R. Thome, Dynamic void fractions in stratified types of flow, Part I: New optical measurement technique, Int. J. Multiphase Flow 30 (2004) 107–124.
[8] O. Baker, Design of pipe lines for simultaneous flow of oil and gas, Oil Gas J. 53 (1954) 185–190.
[9] Y. Taitel, A.E. Dukler, A model for predicting flow regime transitions in horizontal and near horizontal gas–liquid flow, AIChE J. 22 (2) (1976) 43–55.
[10] K. Hashizume, Flow pattern and void fraction of refrigerant two-phase flow in a horizontal pipe, Bull. JSME 26 (219) (1983) 1597–1602.
[11] D. Steiner, Heat transfer to boiling saturated liquids, in: VDI-Wärmeatlas (VDI Heat Atlas), Verein Deutscher Ingenieure, VDI-Gessellschaft Verfahrenstechnik und Chemie-ingenieurwesen (GCV), Düsseldorf, 1993 (Translator: J.W. Fullarton).
[12] O. Zürcher, J.R. Thome, D. Favrat, Prediction of two-phase flow patterns for evaporation of refrigerant R-407C

inside horizontal tubes, Convective Flow and Pool Boiling Conference II, Paper IX-I, Isree, May 18–23, 1997.

[13] J.R. Thome, J. El Hajal, Two-phase flow pattern map for evaporation in horizontal tubes: Latest version, in: 1st Int. Conf. on Heat Transfer, Fluid Mechanics and Thermodynamics, Kruger Park, South Africa, April 8–10, vol. 1, 2002, pp. 182–188.

[14] D. Biberg, An explicit approximation for the wetted angle in two-phase stratified pipe flow, Canadian J. Chem. Eng. 77 (1999) 1221–1224.

[15] H. Mori, S. Yoshida, K. Ohishi, Y. Kokimoto, Dryout quality and post dryout heat transfer coefficient in horizontal evaporator tubes, in: Proc of 3rd European Thermal Sciences Conference, 2000, pp. 839–844.

[16] J.G. Lavin, E.H. Young, Heat transfer to evaporating refrigerants in two-phase flow, AIChE J. 11 (6) (1965) 1124–1132.

[17] S.S. Kutateladze, On the transition to film boiling under natural convection, Kotloturbostroenie 3 (10) (1948).